



# Direct measurement of the effective properties of an additively manufactured titanium octet truss unit cell using high energy X-ray diffraction

Nathan S. Johnson <sup>a,b,\*</sup>, Maria Strantza <sup>c</sup>, Manyalibo J. Matthews <sup>c</sup>, Jun-Sang Park <sup>d</sup>, Peter Kenesei <sup>d</sup>, Bjørn Clausen <sup>b</sup>, Donald W. Brown <sup>b</sup>, John S. Carpenter <sup>b</sup>, Craig A. Brice <sup>a</sup>, Aaron P. Stebner <sup>e</sup>

<sup>a</sup> Colorado School of Mines, Golden, CO 80401, United States of America

<sup>b</sup> Los Alamos National Laboratory, Los Alamos, NM 87545, United States of America

<sup>c</sup> Lawrence Livermore National Laboratory, Livermore, CA 94551, United States of America

<sup>d</sup> Argonne National Laboratory, Lemont, IL 60439, United States of America

<sup>e</sup> Georgia Institute of Technology, Atlanta, GA 30332, United States of America



## ARTICLE INFO

### Keywords:

Octet truss  
Lattices  
Octet truss lattice  
Additive manufacturing  
Advanced characterization  
X-ray  
Diffraction  
X-ray diffraction  
Synchrotron  
In situ  
Mechanical  
Mechanical characterization

## ABSTRACT

Additively manufactured lattice structures offer a high specific strength-to-density ratio in comparison to conventional, fully dense parts. The small feature size and intricate geometry of lattice structures make it challenging to directly characterize their mechanical properties. This study presents direct measurement of the elastic mechanical properties of an additively manufactured titanium alloy octet truss unit cell. Strut stress and strain were measured using high-energy X-ray diffraction during quasi-static compressive loading. The crystallographic stress-strain relationship was converted into the stress-strain relationship of the octet truss lattice unit cell using the known symmetry of the struts. The sample studied herein was best fit by an orthorhombic linear elastic stress-strain relationship. This technique shows promise for studying additively manufactured lattice structures at length scales not previously reported.

## 1. Introduction

Lattice structures have many applications as low density, load bearing parts that provide comparable mechanical properties to fully dense material. Lattice structures are used in biomedical devices [1–4], aerospace components [5,6], automotive parts [7], energy absorption [8,9], heat exchangers [10], and more. The octet truss is a lattice topology that disperses compressive load primarily through stretching [11,12]. Recent advances in additive manufacturing have enabled manufacturing of single-component octet truss lattices with millimeter (and smaller) sizes [13–15]. Highly engineered lattice features present new opportunities for structural applications. However, it also creates new challenges for characterization and validation.

Traditional studies of octet truss lattices have mechanically tested

their macro scale properties by compressing, stretching, or bending a component containing many unit cells. In these studies, strain is measured by extensometer and stress values are converted from the force measured on load cells [16–19]. While these are accurate methods for characterizing the macroscopic behavior of many-unit cell octet truss lattice structures, they cannot observe the behavior at the sub-unit cell scale.

Although robust predictions exist for the properties of octet trusses on the unit cell scale [11], few studies have investigated the properties of individual struts themselves. The behavior of the unit cell in a lattice material is important for development of homogenization schemes that accurately and efficiently model the macroscale behavior of a lattice part [15,20,21]. We aim to study the properties of the octet truss under compression at the unit cell level and compare the stress-strain results

\* Corresponding author at: Colorado School of Mines, Golden, CO 80401, United States of America  
E-mail address: [nathan.johnson@zeiss.com](mailto:nathan.johnson@zeiss.com) (N.S. Johnson).

with current models for the geometry.

In this study, we present direct measurements of the elastic mechanical behavior of an unconstrained octet truss unit cell under compression. High energy X-ray diffraction was used to measure the crystallographic elastic strain of additively manufactured Ti-5553 octet truss lattices in-situ during quasi static compression. The measured crystallographic strains are then converted into stresses. The overall stress strain behavior of the unit cell is presented and compared to continuum level models of octet truss lattices [11]. The mechanical behavior observed matches closely with other investigations as well as the continuum mechanical framework of Deshpande, Fleck, and Ashby [11]. This indicates that high energy X-ray diffraction is a useful, reliable tool for studying complex lattice structures on the unit-cell level scale.

## 2. Materials and methods

Octet truss unit cells were manufactured by selective laser melting (SLM) out of Ti-5Mo-5 V-5Hf-3Cr (Ti-5553) powder. Ti-5553 is a nominally single phase near- $\beta$  Ti alloy with a lattice parameter of approximately  $3.2412\text{\AA}$  [22]. It has found uses in aerospace applications [23] due to its high hardness and strength, coupled with low density [24]. More recently Ti-5553 has found promise as an alloy for additive manufacturing of structural materials [22,25].

The octet truss unit cell is akin to a face-centered cubic structure where the endpoints of the struts (the nodes) occupy the face centered sites. The sample tested was two unit cells tall and one unit cell wide. The sample in this work had a nominal strut thickness of  $t = 0.495$  mm and length of  $a = 5.715$  mm. Using the density definition of Deshpande, Fleck and Ashby, this sample has a unit cell density of  $\bar{\rho} = 20\%$  [11].

Eight independent struts were monitored during compressive deformation and are labeled in Fig. 1. Given the complicated geometry of the sample and the 3dimensional nature of the measurements, it is important to explain how plots of the resultant data were constructed. Fig. 1a shows the locations measured using high energy X-ray diffraction colored in (1) orange, (2) dark green, (3) light green, (4) navy blue, (5) brown, (6) pink, (7) red, and (8) purple. The orientation of the sample on the build substrate is shown in Fig. 1b. Images of the sample, with the struts highlighted by their corresponding colour, can be seen in Fig. 1 (c-e).

### 2.1. Printing parameters and heat treatment

Samples were printed on an SLM Solutions SLM 280 printer using Ti-5553 powder feedstock. Powder characteristics are shown in Table 1.

Table 1 also lists the relevant printing parameters, including laser power and scan speed. The part was manufactured using three sets of scan parameters; the baseplates (bulk) and struts were manufactured with different parameters to account for their different feature sizes. The strut portion also had a skin layer applied to help reduce surface roughness.

The samples were subjected to ultrasonic cleaning after manufacture, then heat treated for stress relief at  $300\text{ }^{\circ}\text{C}$  for one hour in vacuum ( $10^{-5}$  mbar) while still on the build substrate. The ramp up and ramp down time of the stress relief was  $16\text{ }^{\circ}\text{C}$  per minute. Samples were cooled in Argon until they reached  $90\text{ }^{\circ}\text{C}$ . After heat treatment, samples were removed from the baseplate using electro discharge machining.

It is important to note the orientation of truss members relative to the build, recoater blade, and heat flow directions shown in Fig. 1(b). Some of the trusses are oriented flat on the substrate and should experience

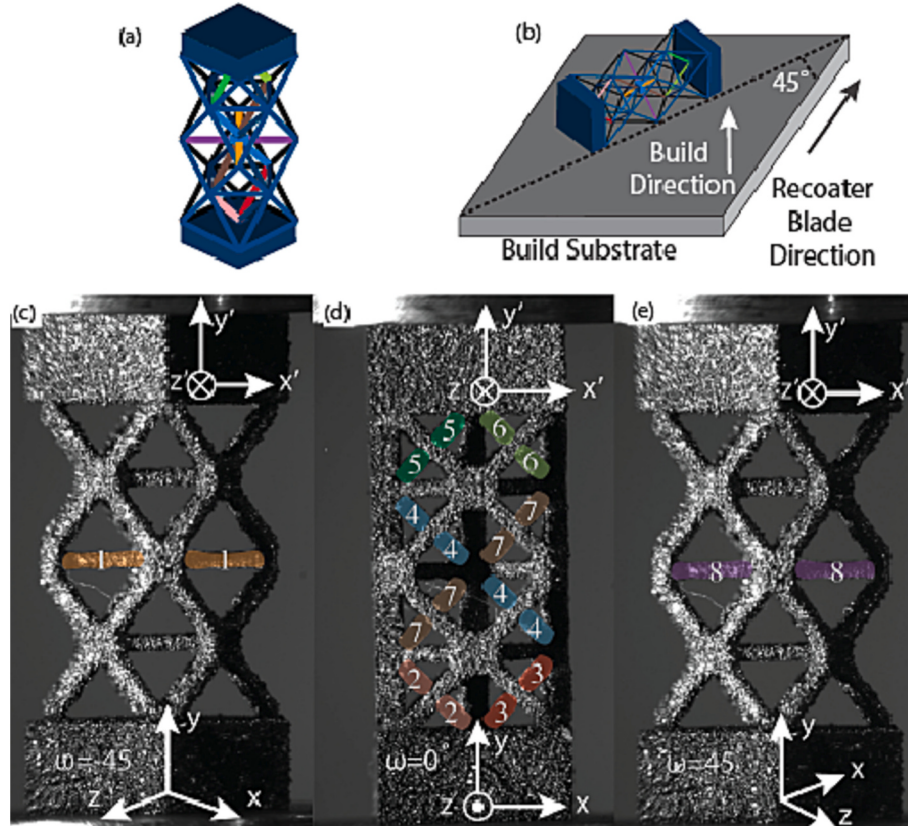


**Fig. 1.** Explanation of locations measured on the sample. (a) A diagram of the sample. The struts that were measured are highlighted in various colors. (b) The orientation of the sample on the build substrate during printing. (c-e) The sample at  $\omega = -45^{\circ}$ ,  $0^{\circ}$ , and  $45^{\circ}$ . The laboratory and octet truss coordinate frames are shown at the top and bottom of the sample, respectively. The struts that were measured are highlighted and labeled at each orientation. The colors used on this plot for each individual strut will be maintained throughout the remainder of the article.

**Table 1**

Sample powder characteristics, powder composition, and printing parameters. Composition is reported in weight percent.

Alloy		Supplier		Powder size		
Ti-5553		AP&C, a GE additive company			20–63 $\mu\text{m}$	
O (max)	N (max)	C (max)	H (max)	Fe	Al	V
0.1	0.008	0.019	0.003	0.39	5.32	5.0
Mo	Cr	Zr	Y	Be	Ti	
4.88	2.99	$\leq 0.002$	$\leq 0.001$	$\leq 0.001$	Balance	

Location	Scan speed (mm/s)	LaserPower (W)	Hatch Spacing (mm)	Layer Height ( $\mu\text{m}$ )
Baseplate	725	175	0.12	30
Strut	800	100	0.12	30
Skin	525	100	0.12	30

approximately equal heating and cooling cycles during building. Other members are extended at a 45° angle to the build direction. These struts may experience different heating and cooling rates in different locations over the course of the build. This distinct thermal profile is known to cause residual stress buildup in the sample [26].

## 2.2. Mechanical loading and high energy X-ray diffraction

High-energy X-ray diffraction experiments were conducted at the 1-ID beamline of the Advanced Photon Source, Argonne National Laboratory. A diagram of the experimental setup can be seen in Fig. 2. A 71.68 keV box beam of size  $100 \times 100 \mu\text{m}^2$  was used for transmission X-ray diffraction. A diagram of the experimental setup is shown in Fig. 2. The incident beam impinged on specified locations on the sample and scattered onto a Dexela 2923 CMOS detector with 3888×3072 pixels with edge length of 78  $\mu\text{m}$  [27]. Diffraction patterns were collected for

0.1 s at each location.

The sample was scanned across the X-ray beam in 45  $\mu\text{m}$  steps. The size of the beam relative to a strut and step size can be seen in the upper left hand side of Fig. 2. Diffraction images were spotty and far from a ‘powder’ diffraction condition. Therefore, images were summed over 450  $\mu\text{m}$  regions on each strut to improve statistics, which corresponds to taking the sum of every 10 images obtained along a strut. Each individual location shown on plots such as Fig. 1(c) corresponds to an area of 450  $\mu\text{m}$ .

The experimental setup allowed full diffraction rings to be collected with a  $d$ -spacing range of 0.9–4  $\text{\AA}$ . Ti-5553 has a body centered Bravais lattice with an  $\text{Im}\bar{3}$  m space group and an average lattice parameter of 3.2412  $\text{\AA}$ . The observed reflections were the {110}, {200}, {211}, {220}, and the {310} planes.

Samples were loaded quasi-statically in increments of 25  $\mu\text{m}$  at a displacement rate of 0.006 mm/s using a custom load frame developed by the Advanced Photon Source and collaborators [28]. The outside of the sample was not pinned or constricted in any way during loading. A small amount of vacuum grease was added to the baseplates to reduce friction between the loadframe platens and sample.

Loading the sample caused deformation and movement of the struts at each load step. The movement of the struts had to be tracked to ensure that scans were taken on the center of the strut. To do so, the positions of the nodes were tracked throughout the experiment. X-ray radiography was used to find the node locations after each load increment. The coordinates of the nodes were then used to compute the straight-line path from node to node. This straight line path was used to locate the struts into the beam path. Displacement steps were taken until the struts deformed to a degree that prevented accurate data collection.

The detector position and orientation was calibrated using a sample of nanocrystalline Cerium Oxide ( $\text{CeO}_2$ ) in GSAS-II [29].

## 2.3. Ex situ characterization

A full 3D X-ray computed tomography scan of the sample was taken before and after in situ loading. X-ray computed tomography was performed on a Zeiss Xradia 510 with an isotropic voxel width was 7  $\mu\text{m}$ . The smallest detectable defect width was 14  $\mu\text{m}$ . Sample tomographies

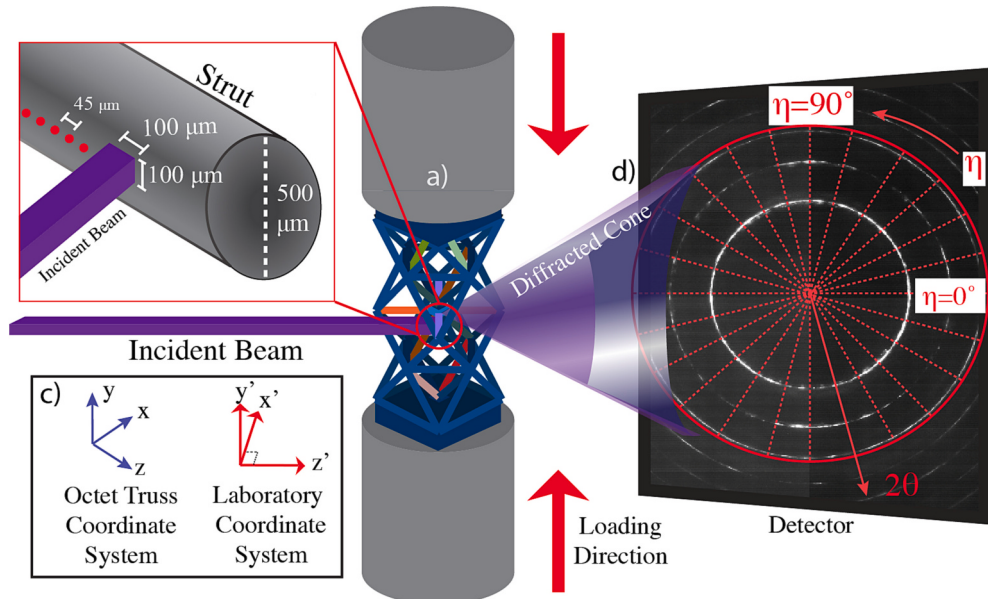


**Fig. 2.** Explanation of locations measured on the sample. (a) A diagram of the sample. The struts that were measured are highlighted in various colors. (b) The orientation of the sample on the build substrate during printing. (c-e) The sample at  $\omega = -45^\circ$ ,  $0^\circ$ , and  $45^\circ$ . The laboratory and octet truss coordinate frames are shown at the top and bottom of the sample, respectively. The struts that were measured are highlighted and labeled at each orientation. The colors used on this plot for each individual strut will be maintained throughout the remainder of the article.

were reconstructed from images and processed for pore density using the Dragonfly Software [30]. A second, nominally identical sample was manufactured on the same baseplate with the same parameters in Table 1 and subjected to the same post-processing. The second sample was then ground and polished for scanning electron microscopy to investigate microstructure.

Diffraction images were taken using the same beamline setup of both the bulk and strut portions of the sample to characterize the texture. Images were taken at the topmost node (where struts 5 and 6 meet) and the left side of strut 1 (strut). The bulk portion was rotatable, allowing for diffraction images to be taken from multiple orientations, while only one orientation could be obtained for the strut due to geometric and physical constraints. Single diffraction images have been successfully used to refine texture, as demonstrated in Ischia et al. [31], and the peak statistics of the diffraction images obtained for these samples are comparable to those used by Ischia. Spherical harmonic functions were used to fit the texture in GSAS II without assuming any symmetry. The spherical harmonic coefficients were then imported into MTEX software for Matlab [32] and used to generate (110) pole figures.

#### 2.4. Coordinate frames

The following discussion will use two coordinate frames: the octet truss coordinate frame ( $x, y, z$ ) and the laboratory coordinate frame ( $x, y, z$ ). Both are shown in Fig. 2(c).

The laboratory coordinate frame is a fixed coordinate frame with the  $+z$  direction oriented parallel to the incident X-ray beam with  $+y$  vertical and  $+x$  making a right-handed coordinate system. Note that  $y$  and  $y'$  are parallel. The diffracted cone intersects with the detector in the  $x - y$  plane. A polar angle  $\eta$  is also defined in the  $x' - y'$  plane, shown in Fig. 2(e), to describe polar orientation around the detector.

Loading occurs in the  $y'$  direction and the sample is rotated in the  $\omega$  direction around the  $y$  axis. The sample was rotated so that different struts could be placed in the X-ray beam on the  $x - y$  plane.

The octet truss coordinate frame is defined so that nodes – the place where struts intersect – fall onto either the  $x$ ,  $y$ , or  $z$  axis. Loading occurred on the  $y$  axis. The sample is expected to compress in the  $y$  direction and expand in the  $x - z$  plane.

The setup of the experiment allowed for measurement of 8 separate struts oriented at various angles in the ( $x, y, z$ ) coordinate frame. Measurements of the orange and purple struts, shown in Figs. 1(c) and (e) respectively, correspond to measurement in  $x - z$  plane of the octet truss. Strains in all the other struts, shown in Fig. 1(d), correspond to measurement in the  $x - y$  plane of the octet truss coordinate system.

#### 2.5. Data preparation

Each diffraction image was divided into 24 bins covering  $15^\circ$  of the full diffraction ring around the coordinate  $\eta$ . The detector image in Fig. 2(e) shows the  $\eta$  direction and bin regions. Each bin was integrated to produce a diffraction histogram for each  $\eta$  angle.

The individual  $\eta$  direction histograms were integrated and refined with Rietveld Refinement using GSAS [33] and the SMARTSware routine [34]. This refinement produced a crystal lattice parameter  $a_\eta^\ell$  where  $\eta = 0^\circ, 15^\circ, \dots, 345^\circ$  is the integration bin and  $\ell = 0 \mu\text{m}, 25 \mu\text{m}, 50 \mu\text{m}, \dots, 380 \mu\text{m}$  is the crosshead displacement in compression at each load step. This method for calculation of the polar lattice parameter has been used extensively before [35,36].

#### 2.6. Calculation of strain and stress

The goal of the experiment is to measure mechanical behavior during loading and calculate effective material constants of the octet truss unit cell like the elastic moduli. The stress and strain calculated from the  $d$ -spacing are used to calculate these effective properties.

The strain  $\epsilon$  was calculated from the crystal lattice parameter  $a$  for each loadstep  $\ell$  and  $\eta$  direction using

$$\epsilon_\eta^\ell = \frac{a_\eta^\ell - \bar{a}_0}{\bar{a}_0} \quad (1)$$

where  $\bar{a}_0$  is the lattice parameter at zero load averaged over all orientations of all struts, given by

$$\bar{a}_0 = \frac{1}{24} \sum_{\eta=0^\circ}^{360^\circ} a_\eta^0 \quad (2)$$

where the sum is taken over all 24  $\eta$  bins. In this experiment we found an average lattice parameter of  $\bar{a}_0 = 3.2412 \text{ \AA}$ .

One important aspect of this investigation was to find the value and orientation of *principal strains* in the sample. The principal tensile  $\epsilon_1$  and compressive  $\epsilon_2$  strains are the highest magnitude strains at a given location.

The principal strains were fit using the method of I.C. Noyan and J.B. Cohen [35], which has been used in similar investigations [37], given by

$$\epsilon_\eta^\ell = \epsilon_1^\ell \sin^2(\eta + \psi) + \epsilon_2^\ell \cos^2(\eta + \psi) \quad (3)$$

where  $\psi$  is the orientation, in degrees, of the principal coordinate system relative to  $\eta = 0^\circ$  in the ( $x, y, z$ ) coordinate system.

The full model of Noyan and Cohen includes shear terms and a third strain component  $\epsilon_{33}$  but in the current experiment only two strain components ( $\epsilon_x$  and  $\epsilon_y$ ) could be measured at a single time. In order to calculate a stress, however, assumptions about the third strain component had to be made.

The third strain component was set as equal to either the  $\epsilon_1$  or  $\epsilon_2$  strain depending on the measurement location. Struts transverse to loading should deform primarily in tension; thus, by Poisson's effect, the other two strains should be compression. Therefore, struts 1 and 8 in Fig. 1 were assumed to have  $\epsilon_3 = \epsilon_2$ . The remaining struts are oriented  $45^\circ$  off the loading direction and should deform primarily in compression, thus the remaining two strains should be tensile. These struts were assumed to have  $\epsilon_3 = \epsilon_1$ . In all cases, the direction of the third strain component was defined so that it formed a right-handed coordinate system with  $\epsilon_1$  and  $\epsilon_2$ .

The Young's modulus  $E_s$  and Poisson's ratio  $\nu_s$  of the material must also be known to calculate a stress. Calculating  $E_s$  and  $\nu_s$  requires knowledge of the bulk stress and strain in the sample.

$E_s$  and  $\nu_s$  were measured from a sample of Ti-5553 manufactured using the strut printing parameters in Table 1 and printed on the same substrate. The sample was a  $2 \text{ mm} \times 2 \text{ mm} \times 2 \text{ mm}$  cube sectioned out of a larger  $25.4 \text{ mm} \times 25.4 \text{ mm} \times 25.4 \text{ mm}$  cube. Sectioning out the small cube from the larger cube relieves long-range internal stresses that build up during printing [38], thus providing a residual stress-free measurement of the material constants.

The sample cube was loaded quasi-statically in steps of  $25 \mu\text{m}$  using the same procedure detailed in Section 2.2. The lattice parameter was measured during loading and converted into a strain. Since the surface area of the reference cube was known, along with the applied force from the load cell, a macroscopic stress on the sample could be calculated.  $E_s$  and  $\nu_s$  were calculated from the slope of the stress-strain plot. A Young's modulus of  $E_s = 48.35 \text{ GPa}$  and Poisson's ratio of  $\nu_s = 0.326$  were measured. This is in good agreement with values found by other investigations [39].

Once the material constants were measured the stress was calculated as

$$\sigma_{ii}^\ell = \frac{E_s}{1 + \nu_s} \epsilon_i^\ell + \frac{\nu E_s}{(1 + \nu)(1 - 2\nu_s)} \text{tr}(\epsilon^\ell) \quad (4)$$

where  $\text{tr}(\epsilon) = \epsilon_{11} + \epsilon_{22} + \epsilon_{33}$  [35].

Strains were first calculated and fit using Eqs. 1 and 3. These equations provide the principal  $\epsilon_1$ ,  $\epsilon_2$  and  $\epsilon_3$  strains that can be converted to

stresses  $\sigma_1$ ,  $\sigma_2$  and  $\sigma_3$  using Eq. 4. Principal strains need to be transformed to the octet truss coordinate system defined in Fig. 2c. The transformation is a rotation from the principal coordinates to the octet truss coordinates ( $x, y, z$ ) using Eq. 3.

## 2.7. Calculation of effective constants for the octet truss unit cell

A 2001 paper by Deshpande, Fleck, and Ashby lay out a theoretical framework for the stress-strain relationship in the octet truss. Under the assumption that all nodes are pinned, the octet truss unit cell should obey an isotropic linear elastic relationship given by

$$\begin{bmatrix} \epsilon_x \\ \epsilon_y \\ \epsilon_z \\ \epsilon_{xy} \\ \epsilon_{yz} \\ \epsilon_{xz} \end{bmatrix} = \begin{bmatrix} s_1 & -s_2 & -s_2 & 0 & 0 & 0 \\ s_1 & -s_2 & 0 & 0 & 0 & 0 \\ s_1 & 0 & 0 & 0 & 0 & 0 \\ s_3 & 0 & 0 & s_3 & 0 & 0 \\ s_3 & 0 & s_3 & 0 & s_3 & 0 \\ s_3 & s_3 & s_3 & 0 & 0 & 0 \end{bmatrix} \begin{bmatrix} \sigma_x \\ \sigma_y \\ \sigma_z \\ \sigma_{xy} \\ \sigma_{yz} \\ \sigma_{xz} \end{bmatrix} \quad (5)$$

where  $\epsilon$  and  $\sigma$  are in the octet truss coordinate frame [11]. The stiffness constants  $s_i$  are nominally related to the material Young's modulus as

$$\begin{aligned} \frac{1}{s_1} &= \frac{\hat{\rho}E_s}{9} \\ \frac{1}{s_2} &= \frac{\hat{\rho}E_s}{3} \\ \frac{1}{s_3} &= \frac{\hat{\rho}E_s}{12} \end{aligned} \quad (6)$$

where  $\hat{\rho} = 0.2$  is the density of the octet truss unit cell. The validity of Eq. 6 is based on the assumption of uniaxial loading and pin-jointed nodes.

In our study we are looking only at a single unit cell. The nodes on the top and bottom of the structure ( $\pm y$ ) are pinned but all other nodes are free to deform. As such, the condition of isotropic symmetry was relaxed.

Instead, several different linear elastic relationships were fit to the measured stress-strain behavior. The goodness of-fit of was determined by the correlation  $R^2$  between the measured stress/strain and the values produced from fitting. All possible linear elastic symmetries were fit, from triclinic through isotropic.

Fitting the linear-elastic relationship of the unit cell requires transforming the stress and strain into the octet truss ( $x, y, z$ ) principal coordinate system. Struts 1, 4, 7, and 8 were chosen for fitting the linear elastic relationship because they all have the same node conditions. Struts 2, 3, 5 and 6 are pinned at the top and bottom of the sample and are expected to deform differently than those in the center of the sample that are not pinned.

Measurements of  $\epsilon_x$ ,  $\epsilon_y$ , and  $\epsilon_z$ , and their associated stresses, can obtained from rotations of the principal strains found in Eq. 3. The principal tensile strains on struts 1 and 8 lay in the  $xz$  plane. Separate strain measurements on struts 1 and 8 can be transformed into the  $x$  and  $z$  directions. Likewise, struts 4 and 7 lay in the  $yz$  plane and can be transformed into the  $y$  direction. Thus, we can obtain six strain measurements ( $\epsilon_x, \epsilon_y, \epsilon_z, \epsilon_{xy}, \epsilon_{yz}, \epsilon_{xz}$ ) and their corresponding stresses. These values can be used to test the validity of Eq. 5, or any other linear elastic stress-strain model.

## 2.8. Sources of uncertainty and uncertainty propagation

The analysis above assumes that variation in the crystal lattice parameters occurs solely due to the applied force. However, there are several phenomena that can cause variation in the crystal lattice parameter.

Segregation or partitioning of the alloying elements (Mo, V, Hf, Cr) can cause local distortions in the unit cell, resulting in a slightly different lattice parameter for any grain that is rich or depleted in any element.

Although a secondary phase was present in some parts of the material, as discussed later, its volume fraction was <1% and thus not expected to have a significant impact on the lattice parameter.

In order to accurately measure the lattice parameter precise knowledge of the sample-to-detector distance is necessary. If the sample moves relative to the detector (in the  $z$  direction) due to compliance, slippage, or buckling, then it will appear as though the lattice parameter has changed.

A sample of CeO<sub>2</sub> was used to measure the change in lattice parameter as a function of sample-to-detector distance. The CeO<sub>2</sub> was scanned in the  $z$  direction in steps of 100 μm and the lattice parameter was measured at each step. The lattice parameter sensitivity to sample detector distance was found to be 0.0263°A/mm of displacement. This means a 1 mm displacement in the sample will appear as a lattice parameter change of 0.0263.°A.

The location of the sample's nodes was tracked during measurement as described in Section 2.2. The node coordinates at each loadstep were used to estimate the lattice parameter uncertainty due to displacement. The largest node displacement was 200 μm over the course of the entire experiment, corresponding to an apparent change in lattice parameter of 0.00526°A. Therefore, a lattice parameter uncertainty of ±0.00526°A was propagated through all equations. Propagation of uncertainty was calculated using the usual methods [40].

## 3. Results

### 3.1. Microstructure

Fig. 3 shows the microstructural characterization of the sample, with grain sizes ranging from a few microns in the smallest grains to around 75 μm in the largest. Additionally, several voids about a micron wide were present in the microstructure (indicated by red circles in Fig. 3a).

Fig. 3(c) highlights examples of diffraction peaks from an unexpected secondary phase observed at some locations in the samples. The secondary phase has low intensity, broad peaks that are indicative of a small grain size and was primarily observed in the bulk regions of the samples, such as at the nodes or in the top and bottom baseplates. It is possible that the phase was also present in the strut sections of the sample but was too low intensity to detect.

Zheng et al. previously observed a face-centered orthorhombic titanium phase in Ti-5553 when it underwent the same heat treatment as this study [41]. The secondary phase was refined using the starting lattice parameters reported by Zheng, resulting in a final Pawley refinement with a weighted residual of 9% and lattice parameters  $a = 3.277$ °A,  $b = 4.564$ °A, and  $c = 13.903$ °A.

The (100) pole figures for the bulk and strut are shown in Fig. 3d and e, respectively. The bulk exhibited a weak fiber texture in the build direction which is consistent with previously characterized textures of additively manufactured Ti-5553 [22]. Similarly, the strut also showed a weak fiber texture as shown in Fig. 3e, although the texture was concentrated into several poles instead of being dispersed like the texture of Fig. 3d. The pole density was only 1.6 multiples of random distribution (mrд), indicating a weak texture.

X-ray computed tomography of both the pre-mortem and post-mortem samples is shown in Fig. 3f. Prior to compression, the samples displayed large voids primarily located in the bulk sections of the sample, such as the nodes and base plates, with smaller voids in the struts. After compression, more large voids were observed. The density of the sample, as measured from the tomographs, decreased from 99.95% pre-mortem to 99.61% post-mortem.

### 3.2. Stress and strain characterization with X-ray diffraction

Residual strains were calculated from the lattice parameter using Eqs. 1 and 3. The principal tensile  $\epsilon_1^0$  and compressive  $\epsilon_2^0$  strains fell

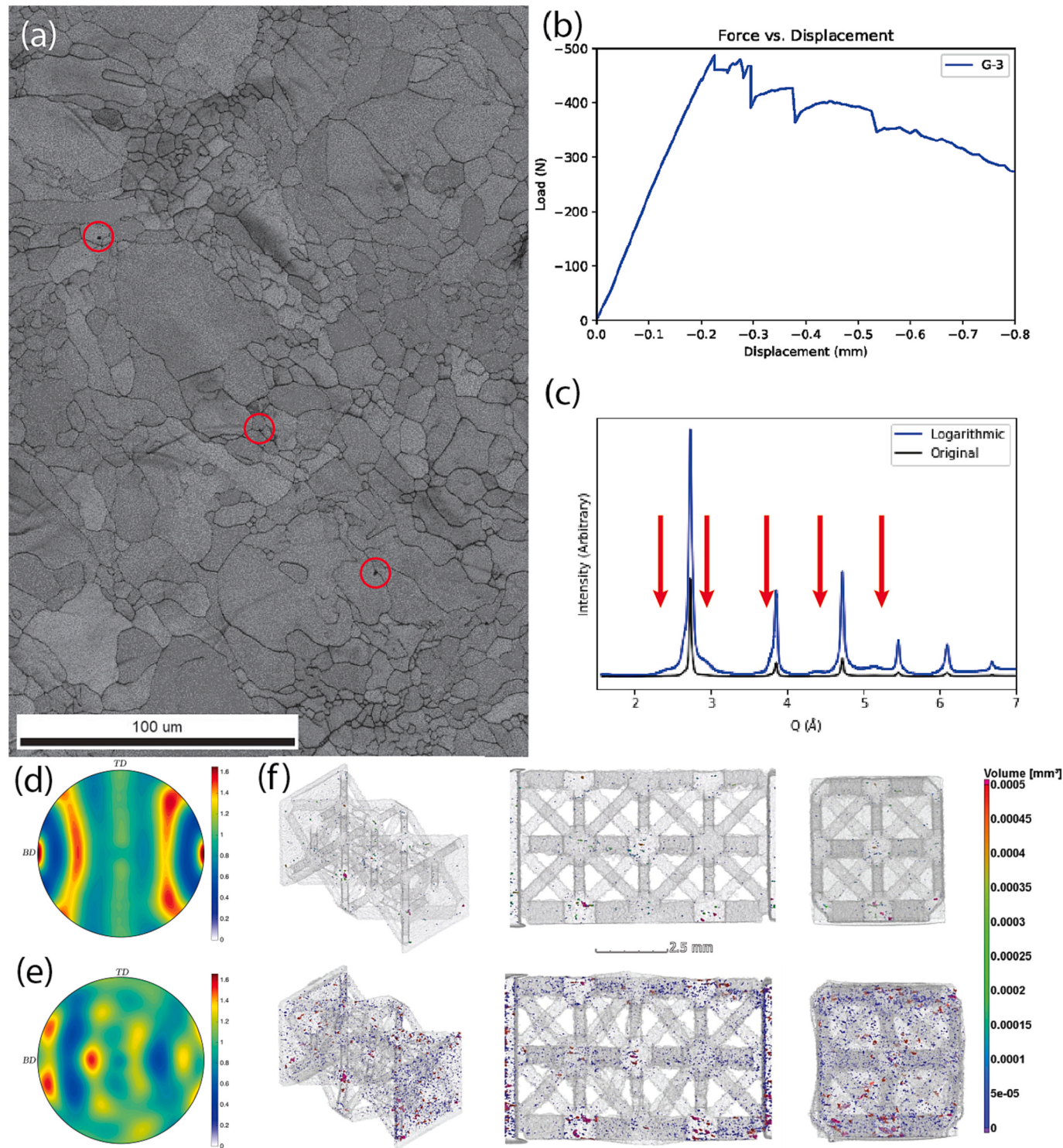


**Fig. 3.** (a) SEM micrograph showing the distribution of grains in the strut portion of the sample. Red circles indicate visible pores. (b) The load-displacement curve for the sample. Diffraction images were collected up to 295  $\mu\text{m}$  of displacement. (c) An example X-ray diffraction histogram from a sample node. Peaks from the secondary phase are highlighted by red arrows. (d) The (100) pole texture taken from the bulk, marked with the build direction (BD) and transverse direction (TD). The BD and TD correspond to the x and y directions, respectively. (e) The (100) pole figure from the strut portion of the sample. (f) X-ray computed tomography of the sample before (top) and after (bottom) compression. (For interpretation of the references to colour in this figure legend, the reader is referred to the web version of this article.)

below the measurement uncertainty ( $<4 \times 10^{-5}$ ) in almost all locations. The largest residual tensile strains were 0.0015 and occurred in mid-sections of Struts 2 and 7. Likewise, struts 2, 4, 5 and 7 showed compressive strains that rose as high as  $-0.0001$ . Overall, the residual strains in the sample were minimal. The distribution of all initial lattice

strains at zero displacement is shown in the Supplemental information.

A load-displacement curve measured from the load cell can be seen in Fig. 3b. The sample exhibited its first fracture at 225  $\mu\text{m}$ , indicated by a dip in load on the load-displacement curve. Further fracture and buckling occurred with further loading.

The principal (compressive and tensile) strain at every displacement step in every strut is shown in Figs. 4 and 5. The bottommost lines in these plots represent the strain across the strut at zero load. Further lines plot the strain at each successive displacement step. Struts are oriented in the plots according to their actual orientation in the sample.

The majority of tensile strains in the sample are concentrated in strut 1 and strut 8 (Fig. 4). Struts 4 and 7 also showed significant tensile strains through loading but did not increase at the same rate as struts 1 and 8. By the end of the experiment (displacement step of 295  $\mu\text{m}$ ) struts 1, 4, 7, and 8 had comparable tensile strains. The highest compressive strains are concentrated in struts 4 and strut 7 (Fig. 5). These struts began showing significant compressive strains at the 100  $\mu\text{m}$  displacement step; this is the same step when struts 1 and 8 began showing significant tensile strains. The magnitude of compression in struts 4 and 7 are roughly the same magnitude as the tensile strains in struts 1 and 8.

Struts 2, 3, 5 and 6 had negligible tensile and compressive strains up to 100  $\mu\text{m}$  of displacement. Starting at 125  $\mu\text{m}$  displacement these struts had some locations with compressive strains above uncertainty. These struts had no tensile strains above the measurement uncertainty even at 200  $\mu\text{m}$  of displacement. The right hand side of strut 2 had negligible tensile and compressive strains for all displacement steps shown.

At 200  $\mu\text{m}$  of displacement the largest tensile strain is 0.0085 (strut 1) while the largest compressive strain is -0.011 (strut 7). Strut 1 has a fairly uniform strain distribution up to 200  $\mu\text{m}$  of displacement. Strut 8, on the other hand, shows a higher tensile strain concentration on one side of the strut. The same is not true with the compressive strains of strut 8.

The compressive strain distribution of struts 4 and 7 are highly non-uniform through the entire experiment. Compressive strains built up closer to the midsection of the struts at early loading steps. By the end of the ex-

The tensile strains in struts 1 and 8 rose at comparable rates to the compressive strains in struts 4 and 7. Starting with 25  $\mu\text{m}$  displacement the tensile strains in struts 1 and 8 and the compressive strains in struts 4 and 7 rose by  $\sim 0.001$  with each displacement step.

The highest magnitudes of strains, whether compressive or tensile, occurred in the midpoints of struts away from the nodes. The strain decreases as much as 1/3 closer to the nodes.

Eq. 3 was also used to determine the orientation of the principal compressive and tensile strains. These orientations are shown for each location on the struts in Fig. 6. The colour of arrows in Fig. 5 corresponds to the highest magnitude principal strain (tensile is blue, compressive is

red). Strut 1 had principal strain orientations also parallel to the strut up until fracture. The tensile strains also dominated in this strut; this indicates the strut was primarily in a stretching mode. The same is mostly true for strut 8, with the exception of the one location that displayed little strain at all. At lower loading steps strut 8 had strain orientations that varied from location to location; by the 100  $\mu\text{m}$  displacement step all of these orientations were nearly parallel to the strut.

The remaining struts show a more complicated picture. Struts 2, 3, 5 and 6 had little strain development at all; all of their principal strains are oriented normal to the strut. This indicates that the struts were not compressing/stretching along the strut axis but instead were more likely buckling. The low strain magnitude of these struts makes strong conclusions difficult to make.

Strut 4 had a strong compressive response but its strain orientations vary from location to location. Strut 4 initially had compressive strains oriented perpendicular to the strut axis; at the 100  $\mu\text{m}$  displacement step some locations begin to have compressive strains oriented parallel to the strut. At higher displacement steps, however, the strain orientations vary between being oriented parallel and perpendicular to the strut axis.

Strut 7, on the other hand, showed a behavior closer to struts 1 and 8. Starting at the 25  $\mu\text{m}$  displacement step almost all strains are oriented parallel to the strut direction. This behavior indicates the strut was primarily compressing directly down the strut axis.

### 3.3. Strut fracture and strain redistribution

A small dip in tensile and compressive strain also occurs in Strut 1 between the 200  $\mu\text{m}$  and 225  $\mu\text{m}$  displacement steps, although no fracture was visible on the sample. It is possible that a partial fracture initiated at this displacement step. Strut 1 fully fractured in tension between load steps 225  $\mu\text{m}$  and 250  $\mu\text{m}$ . There is a noticeable drop off in strut 1 strains between these loadsteps, shown in Figs. 4 and 5.

Strut 8 fractured completely between displacement steps 250  $\mu\text{m}$  and 295  $\mu\text{m}$ , again evidenced by a significant drop in the tensile strain. Interestingly, the fracture location on strut 8 is close to the region that showed almost no compressive/tensile strain at all.

There is a noticeable re-distribution of strains in all other struts after both fractures. Strut 4 shows a relaxation in both tensile and compressive strains after the fracture of strut 1 (between 225  $\mu\text{m}$  and 250  $\mu\text{m}$ ). Fracture of the struts allows for relaxation of the unit cell under load as the sample becomes more compliant with fewer struts to resist compression. After the next load step, however, strut 4 compressive

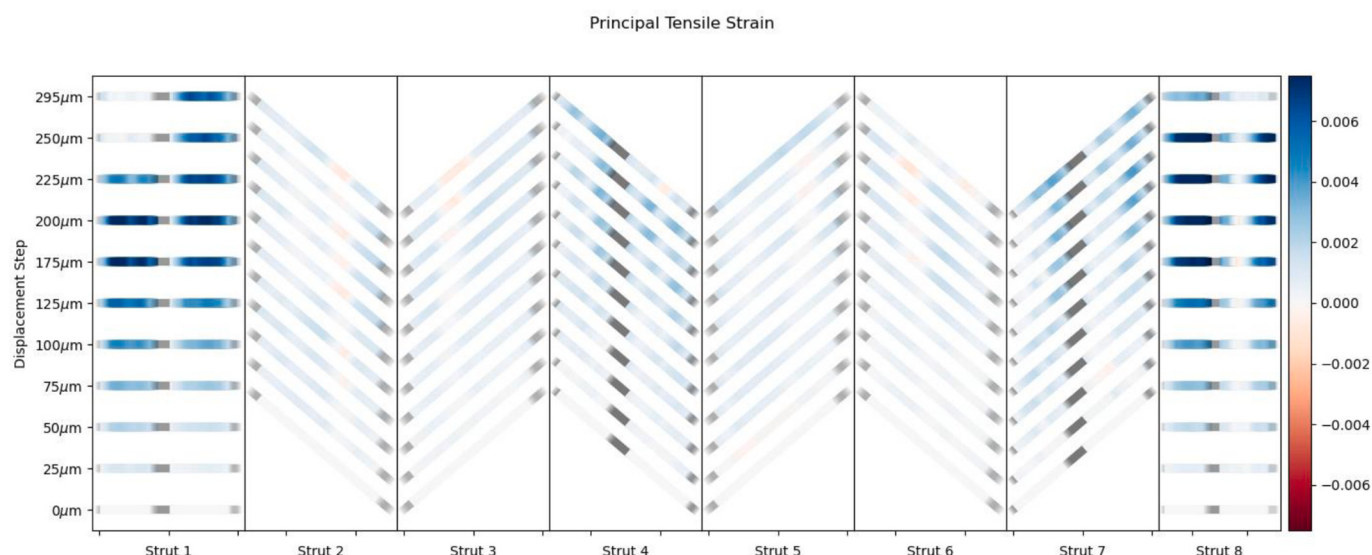


**Fig. 4.** Principal tensile strains (measured from Eq. 3 in all struts at all displacement steps. The angles of the struts correspond to their actual angles in the unit cell. Gray regions on the struts are portions that were not measured because they were blocked by a node or another strut.

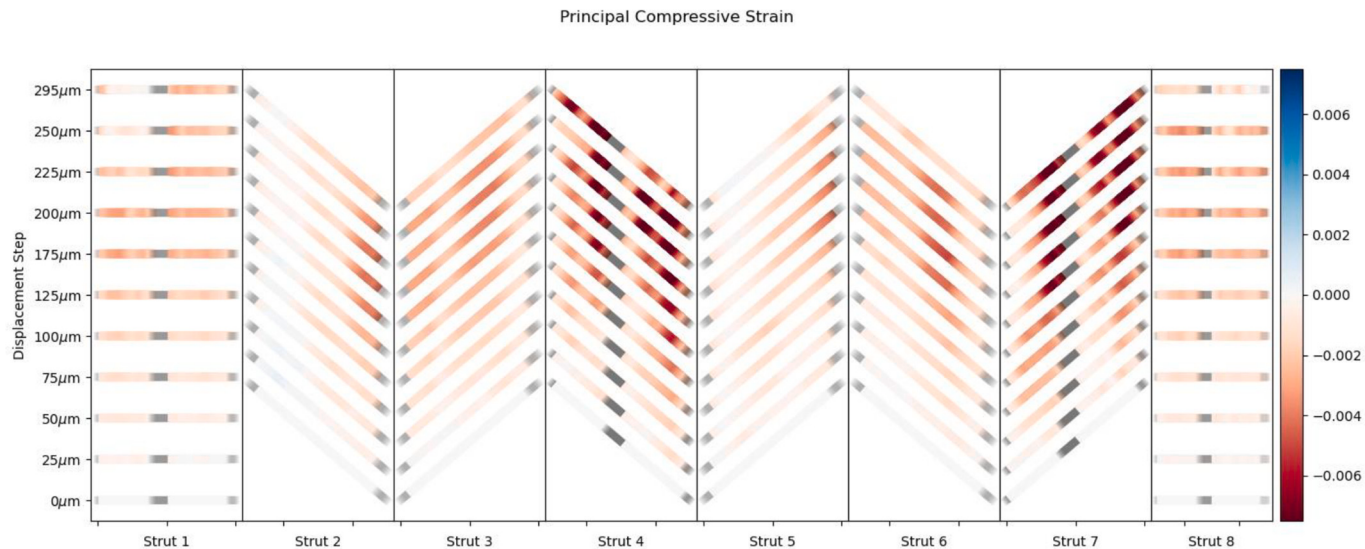


**Fig. 5.** Principal compressive strains (measured from Eq. 3 in all struts at all displacement steps. The angles of the struts correspond to their actual angles in the unit cell. Gray regions on the struts are portions that were not measured because they were blocked by a node or another strut.

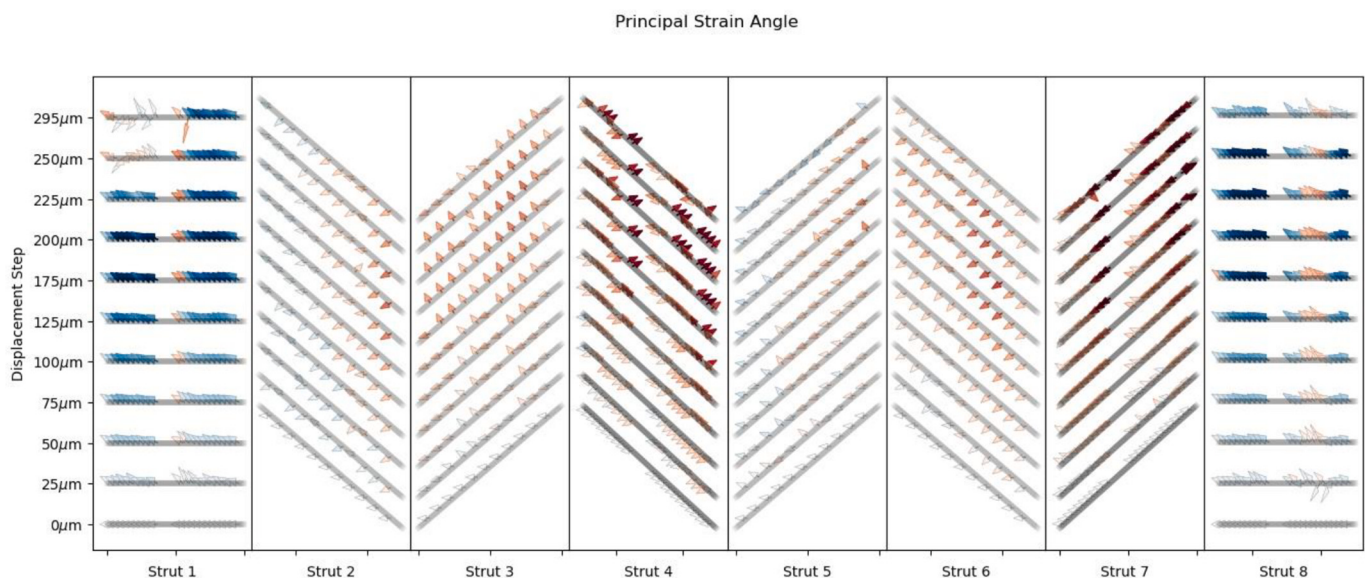


**Fig. 6.** The orientation of the principal strains in all struts at all displacement steps. The direction of the arrows at each location correspond to the direction of the largest magnitude principal strain measured from Eq. 3. Blue arrows indicate the largest magnitude strain at that location was tensile; red indicates compressive. (For interpretation of the references to colour in this figure legend, the reader is referred to the web version of this article.)

strains rose back to their pre-fracture level. A similar behavior occurs after the fracture of strut 8 between the final two displacement steps; the right hand side of strut 4 loses compressive and tensile strain after the fracture of strut 8. The sample was inspected by X-ray CT after loading; strut 4 did not appear to fracture throughout loading. Thus, the drops in strain on this strut are explained by the relaxation of the unit cell.

Interestingly, strut 7 does not show the same behavior as strut 4 even though they are under symmetric loading conditions. Strut 4 does not seem to be affected by the fractures in strut 1 or 8 at all. Instead, strut 7 gains compressive and tensile strains through all displacement steps in the experiment with no drops in strain after fracture.

The redistribution of strain after fracture can also be seen in the principal strain orientations of Fig. 6. Up until the 250 µm displacement step strut 4 has the majority of its compressive strains oriented parallel to the strut axis. After strut 1 fractures the strains on strut 4 reorient; some locations are oriented perpendicular to the strut axis while others

are parallel. This indicates that the primary mode of the strut may have changed from elastic compression to buckling after the fracture occurs.

The crack initiation sites are investigated via optical microscopy of the fracture surfaces, shown in Fig. 7. A full shot of the sample with the broken strut is included in Fig. 7a and b.

Upon initial inspection the failure site appears to be a traditional cup-and-cone fracture caused by stretching and plastic yield of the strut. Analysis at higher magnification, shown in Fig. 7(d) reveals a more complicated picture. There are sites of dimpling and microvoid coalescence in some areas, as well as a large cleavage in the upper right hand side of Fig. 7(d). Whether the sample failed by cleavage on a grain boundary or by plastic yield is unclear. The authors suspect that a combination of both may have occurred. There are apparent facet areas located on the sides of the fracture surface close to the surface of the strut. From the fractographic picture it is revealed that the crack did not initiate from a subsurface internal defect and that it is more likely that it

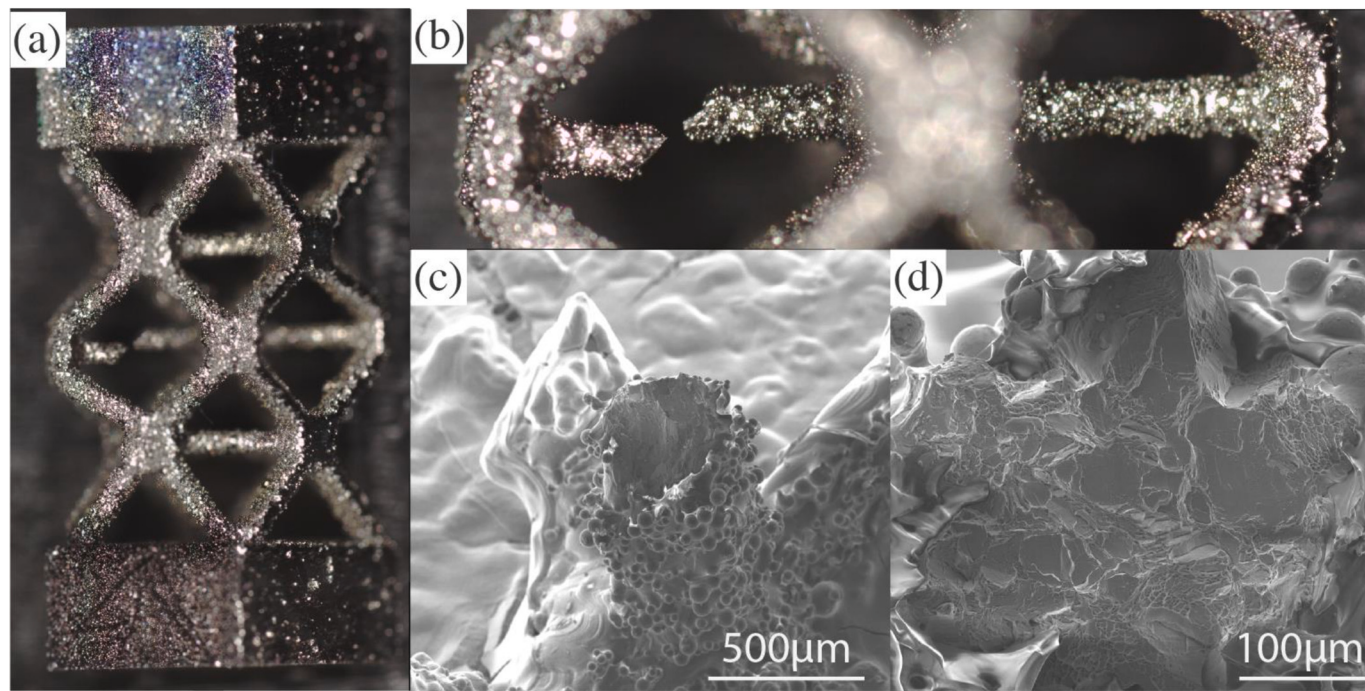


**Fig. 7.** Fractography of the sample. Panels (a) and (b) highlight the first strut to fracture (strut 1). Panels (c)–(f) show the failure point at higher magnifications.

was initiated from local strain concentrations. It is also likely that surface features on the strut caused stress localization that also contributed to failure at this site [15,42].

#### 3.4. The elastic stiffness of different strut orientations

The strains at all displacement steps before fracture, and their corresponding stresses, can be used to understand the overall elastic response of the unit cell. Plots of the tensile and compressive principal elastic stress-strain response in each strut are shown in Fig. 8. Some struts had very low magnitude tensile measurements ( $\leq 0.0005$  strain), or high uncertainties ( $\geq 0.001$  strain), or both. These points are included in Fig. 8, colored in gray, but were excluded from further calculations.

An elastic stiffness was generated from the stress-strain curve for every location on every strut (or at least those with low enough uncertainties). The inset histogram of every plot in Fig. 8 shows all fit values of the elastic stiffness. The average value across locations is shown in red, both in the inset histogram and in the main plots. The value of  $E$  on the plots corresponds to the average stiffness of that strut.

Struts 1 and 8 showed a strong linear elastic stress/strain response in tension. The average stiffness value of these struts was very close to the elastic modulus of the material. The distribution of elastic stiffnesses across these struts has a low standard deviation; all locations demonstrated a stiffness close to the average value with no outliers.

The magnitude of both stress and strain in struts 1 and 8 far exceeds that measured in the remaining struts. Struts 2, 4, 5, and 7 also had a few locations with high tensile strain magnitude and low uncertainty. Struts 2 and 5 showed the highest tensile stiffness; this makes sense considering they are pin jointed at both ends.

Struts 4 and 7, which were not pinned, show a lower tensile stiffness.

Every strut had some locations with low compressive stress/strain uncertainty and high enough magnitude to fit with a line. Struts 1 and 8 both showed a wide distribution in compressive stiffness. The elastic stiffness for these struts varies between 30 MPa and 105 MPa. Locations with a lower moduli were closer to the sample nodes. The regions with higher compressive  $E$  values in these struts are closer to the middle of the struts; lower  $E$  values were closer to the nodes.

Struts 2, 3, 5, and 6 also showed a range of  $E$  values, but not as widely

distributed as strut 1 and 8. These struts tended towards higher compressive  $E$  values, as they did in the tensile case. Again, this can be explained by the pin jointing of these struts.

Struts 4 and 7 performed very similarly in compression as struts 1 and 8 did in tension. Their compressive  $E$  values are both very near the elastic modulus of the material. However, struts 4 and 7 had much higher magnitudes of stress and strain than struts 1 and 8. Strut 7 had the highest measured values of compressive stress and strain across the entire sample at 0.01 and 0.51 MPa, respectively. This can be compared to the highest magnitude tensile stress strains, in strut 8, that only reached 0.0081 and 0.39 MPa, respectively. Even though struts 1 and 8 showed nearly identical tensile stiffness compared to the compressive stiffness of struts 4 and 7, the former struts fractured much sooner than the latter.

#### 3.5. The effective elastic properties of the octet truss unit cell

As discussed in Section 2, the octet truss lattice is usually modeled using an isotropic linear elastic relationship; this is under the assumption that all nodes are pin jointed. This condition is not met in the current study and, as such, further considerations need to be made when modeling the unit cell.

The tensile and compressive strains of struts 1, 4, 7, and 8 were used to generate six strain and stress values in the octet truss coordinate system. These values were then used to perform a linear least squares fit of the compliance tensor of the octet truss.

Four different linear elastic compliance tensors were fit using the values of  $\epsilon$  and  $\sigma$ ; isotropic, tetragonal, and orthorhombic and monoclinic. The hexagonal and trigonal symmetries were not used because they do not fit the geometric layout of the octet truss unit cell. Lower symmetry compliance tensors were also fit but are not reported in this study, as explained below.

A fit of the isotropic linear elastic relationship is shown in Fig. 9. For all stress/strain relationships in Eq. 5 the fit is quite poor. The predicted values are especially off for the compressive stress/strain values; they improve marginally for tensile values.

A similar fit was performed using cubic and tetragonal symmetries; the results are included in the Supplemental information. In summary,

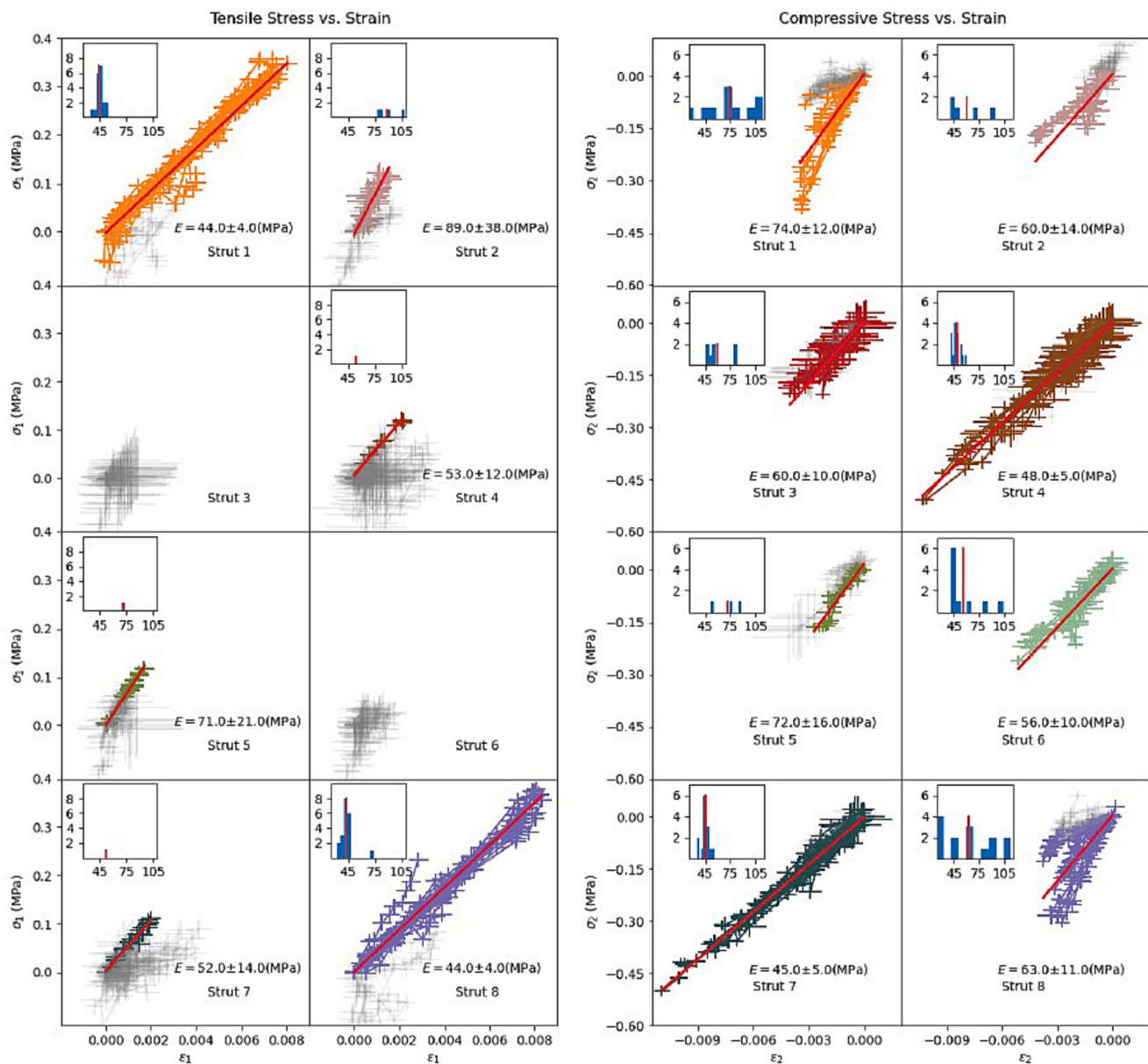


**Fig. 8.** Principal stress and strains measured from Eq. 3 for all struts at all load steps. The left and right hand sides show tensile and compressive strains, respectively. Each individual stress-strain relationship has a line of best fit representing the elastic stiffness. The average elastic stiffness is shown by a red line. Inset histograms show the distribution of all elastic stiffnesses across the strut. The average elastic stiffness is marked on the inset histogram as well. (For interpretation of the references to colour in this figure legend, the reader is referred to the web version of this article.)

the fits of the these symmetry classes performed just as poorly as the isotropic case.

A fit of the orthorhombic linear elastic relationship is shown in Fig. 10. In contrast to the isotropic case, the orthorhombic linear elastic relationship fits the behavior of this sample extremely well. Both in tension and in compression the orthorhombic model predicted the stress/strain values with near perfect accuracy.

#### 4. Discussion

##### 4.1. Impact of printing on microstructure and mechanical properties

The orientation of a part on an additive manufacturing build can cause anisotropy in the mechanical behavior primarily due to induced texture [43–46]. However, in this study, texture played only a minor role in the mechanical performance. The highest pole densities in Fig. 3d

and e were only 1.6 mrd, whereas textures with densities of 10+ mrd are known to cause significant anisotropies in mechanical response [47–49]. The (100) poles in Fig. 3d and e are strongest in the build direction and 45° off the build direction, respectively, which correspond well with the orientations of the struts on the build plate (either 0°, 45°, or parallel to the build direction). The weak texture in the sample can be attributed to the small feature size of the struts; the 500 μm thick struts only require a few layers to print and thus only a few heating-cooling cycles. Larger parts with more heating-cooling cycles may experience more significant texture development.

The print process is also known to induce a gradient of residual strains across the sample along the print direction [38,50]. Some of the only discernable residual strains occurred in Struts 1 and 8 at  $\frac{1}{2}$  and  $\frac{3}{4}$  down the strut. The regions of high residual tensile strain corresponded to regions of high compressive principal strains during loading. The points of failure on struts 1 and 8 also lie at these peaks in residual strain.

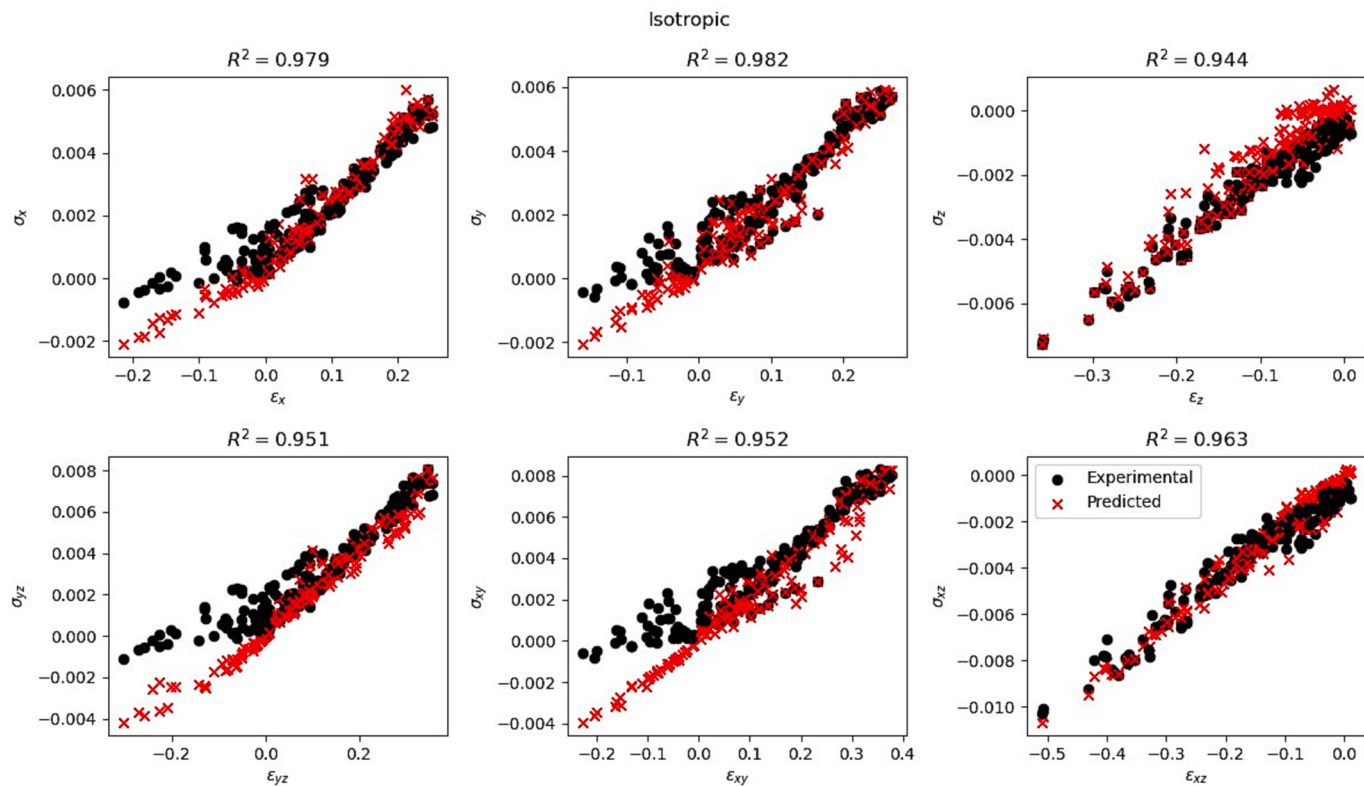


**Fig. 9.** Fits of an isotropic linear elastic stress strain relationship to the principal stresses/strains in the octet truss coordinate system. The  $R^2$  value at the top represents the goodness of fit for this model for each component of Eq. 5.

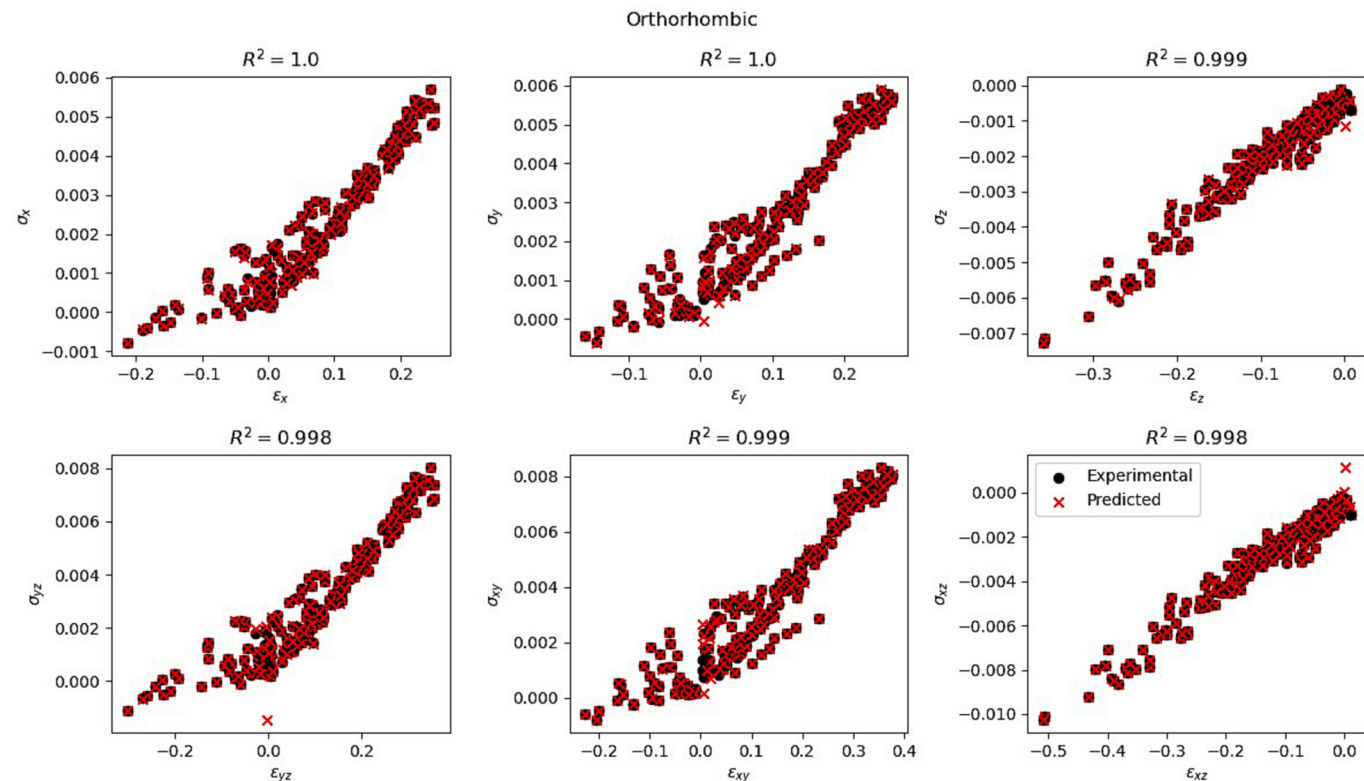


**Fig. 10.** Fits of an orthorhombic linear elastic stress strain relationship to the principal stresses/strains in the octet truss coordinate system. The  $R^2$  value at the top represents the goodness of fit for this model for each component of Eq. 5.

The sample contained a fair amount of voids in the as-heat treated state (0.05% of the density). Voids have been shown to decrease both elongation to failure and ultimate tensile strength during quasi-static loading [51]. CT scans indicate that the volume of voids grew to 0.39% during loading. It is unlikely that new voids were created; rather, the voids were likely below the voxel size of the XCT instrument initially and grew in size during compression.

Voids, however, do not appear to be the cause of failure in Fig. 7 as the fracture site does not show an obvious void where a crack initiated. This is in contrast to previous studies on additively manufactured titanium lattices where Liu et al. found several large pores at the fracture site of struts that failed by plastic yielding [52]. The sample surface was more likely to be the location where a crack was initiated rather than at a subsurface void. Surface roughness reduces the cross-section, creating a stress concentration that initiates cracking.

#### 4.2. The distribution of stress and strain through loading

The octet truss unit cell is designed to disperse the majority of load through stretching of horizontal struts [11]. As compression proceeds, the unit cell is pushed down and the transverse struts are stretched horizontally. The results shown in Fig. 8 confirm this was the case for the present samples. Struts 1 and 8, which are transverse to the loading direction, take on the majority of the tensile strain after only 100  $\mu\text{m}$  of compressive displacement. The principal compressive strain would not match this magnitude until later at 175  $\mu\text{m}$  of displacement in struts 4 and 7. The tensile strain is fairly evenly distributed across Struts 1 and 8 but decreases near the nodes.

Neither strut 4 nor strut 7 showed significantly high residual strains. The reason for their high compressive strains may be due to the boundary conditions on the sample. Struts 2, 3, 5, and 6 are all pinned at the topmost and bottommost nodes of the sample. This confines the ability of these struts to stretch outwards as compression occurs. Struts 4 and 7, located centrally in the sample, are not pinned at any node. As the sample compresses struts 4 and 7 are free to move outward to accommodate the changing unit cell size. In fact, struts 4 and 7 reached compressive strains as high (and higher) in magnitude as the tensile strains of struts 1 and 8.

The sample did not display symmetric stress and strain values across symmetric struts. Based on the geometry of the unit cell, struts 1 and 8 should have experienced the same loading conditions; the same is true for struts 4 and 7. The results shown in Figs. 4 and 5 clearly indicate this is not the case.

Strut 8 has a significant portion that shows no major buildup of either tensile or compressive strains. This is even while neighboring locations have strains as high as 0.008. Strut 1, on the other hand, shows a much more uniform distribution of strain across the strut.

Discrepancies can also be seen in the principal strain orientations of these struts. Strut 1, which showed a near-uniform distribution of tensile strains, also had a near-uniform orientation of strains even in regions that did not have a high strain magnitude.

The regions of strut 8 that had the highest tensile strains also showed strain orientations parallel to the strut, as with strut 1. The other side of the sample had orientations that varied from parallel to the strut, in regions of high tensile strain, or closer to perpendicular from the strut, in regions of high compressive strain.

The same relationship that is true for the symmetric tensile struts (1 and 8) is also true for the symmetric compressive struts (4 and 7). That is to say, one of the struts behaved as expected while the other showed a variety of stress and strain behaviors. Strut 7 behaved as expected and demonstrated a high compressive strain in almost all locations throughout the experiment. Likewise, the orientation of its strains was parallel to the strut axis. Strut 7 was uniformly compressed along its axis throughout the experiment.

Strut 4 also demonstrated high compressive strains throughout the experiment. Its strain orientations, however, varied considerably

throughout the experiment. Some locations changed from being oriented parallel to the strut axis to perpendicular in just one displacement step and without a significant increase or decrease in strain values.

#### 4.3. Comparison with the isotropic Deshpande-Fleck-Ashby model

The results shown in Section 3.5 indicate that this sample did not exhibit an isotropic linear elastic response. Instead, it is better fit by an orthorhombic symmetry. There are several, non mutually exclusive reasons this may be the case.

Isotropic stiffness tensors, such as that laid out in Section 2.7 and in Ref. [11], have two independent stiffness constants; one for the major sample axes ( $x,y,z$ ) and one for the shear directions ( $xy,yz,xz$ ). As discussed previously, the assumption of isotropic properties is for unit cells that are pin jointed at all nodes. This sample was not expected to display an isotropic behavior due to the free nodes at the ends of struts 1, 4, 7, and 8. The authors expected instead that the sample would display a tetragonal linear elastic response whereby the stress-strain response was uniform transverse to the loading direction. This model would have produced separate stiffness constants for the loading direction ( $y$ ) and stretching directions ( $x,z$ ). The shear directions would likewise have their own stiffness constant.

Instead, the sample displayed different stiffness values for all three of the principal octet truss directions, as well as for the shear terms. This orthorhombic response can be clearly seen in distribution of strain values discussed in the previous section. Struts 1 and 8 had different distributions of strains throughout the experiment. While strut 1 was in pure stretching during loading, strut 8 experienced a mix of stretching and compressing.

Residual strains were negligible in the struts at the beginning of the experiment; it is unlikely that residual stress alone caused a non-uniform elastic response. Likewise, crystallographic texture was very low in the sample and is unlikely to cause the observed behavior on its own.

There were voids of significant size in the sample in its as-printed state. More voids grew in the sample throughout loading. Inspection of Fig. 3f shows that the majority of large voids before loading were concentrated in the nodes. Some small voids existed in the struts. The same is true after loading: the majority of voids that nucleated in the sample were concentrated to the nodes. Some small voids did nucleate in the strut region, but not in the same magnitude or number as the nodes. The authors were unable to locate a major void ( $>1 \times 10^{-4} \text{ mm}^3$ ) that nucleated in struts 1, 4, 7 or 8.

The secondary phase present in the sample may also have played a role in the elastic response. Secondary phases that are significantly harder or softer than the primary phase can pin the deformation of other, nearby grains. Even though the diffraction patterns of the secondary phase were too low intensity for a full refinement, the phase was still present in high enough proportion to be noticed at all. This indicates it may have played a non-negligible role in the stress-strain response.

All of these explanations may be minor in and of themselves but can play a major role in the mechanical behavior of the sample when considered in tandem. The authors conjecture that it was not a single defect that caused the orthorhombic response of the sample but rather all defects together.

#### 4.4. Comparison with other measurements of effective properties of the octet truss

The octet truss unit cell has been tested in several materials systems and different loading orientations. Direct comparisons with other investigations can be difficult because they may use a different material, different manufacturing methods, or different loading conditions. One of the more common octet truss samples to test is the snap-fit model [16,17] or 3D printed plastic models [13]. We will compare the general performance of these structures to the behavior found within this study.

Several studies have investigated the impact of heterogeneities on

mechanical behavior in octet truss lattices. Dressler et al. studied a wide range of imperfections in printed individual struts. One of their key findings was that struts printed parallel to the build substrate had higher surface roughness [53]. This has been widely observed before and can be explained by the lack of supporting material under the printed strut, causing a drooping effect [54]. Strut 1 in this study was printed horizontally to the build substrate and was also the first strut to fail. Considering that no major subsurface defects were observed in the fractography (voids or inclusions) a higher surface roughness is a reasonable explanation for its failure.

Jost et al. also discuss impact of heterogeneities on compression behavior of additively manufactured octet trusses. Similar to this study, the observed response deviated from predictions made by the DFA model. Based on the geometry of their samples and the boundary conditions on loading, Jost et al. expected to see clean shear bands dominate be the dominant failure mode of the sample [55]. While shear bands did form, the shear did not occur in a single plane across the sample but instead followed a path with heavy imperfections in the sample. As stated by Jost, the failure of the sample followed the path of least resistance where defects were present.

The snap-fit model of Dong et al. [16,17] featured struts that were twice as long as our struts, or more, and thicker by 3 times or more. Furthermore, the node structure of the snap-fit octet truss lattice is quite different than the 3D printed structure used here. Dong tested this structure on both Ti-6Al-4 V struts [16] and carbon composites [17]. Dong et al. found that for sample densities below 5% elastic buckling tended to be the favored method of failure; above 5% failure by plastic yield dominated [16]. The samples studied herein had a density of 20% and matched this trend; plastic yielding during stretch was the first failure (in struts 1 and 8), followed by elastic buckling after further loading. The behavior observed for the Ti-6Al-4 V snap-fit octet trusses was well replicated on composite samples also studied by Dong, with the primary difference being struts failing by delamination instead of plastic yield [17].

Dong et al. assume an isotropic material model and finds equivalent elastic moduli when loading in the x and z directions (or 11 and 33 directions in Dong's nomenclature) [17]. Our study varies from this behavior and found different elastic responses in the two transverse directions.

Our measurements are on the same order of magnitude as other studies of titanium parts with similar unit cell sizes and strut thicknesses. Liu et al. found a maximum compressive stress of around 500 MPa with a strut thickness of 500  $\mu\text{m}$  [52]. Our study found a maximum value of 450 MPa. Liu's samples also featured similar microstructural features as ours, such as a high density of pores and a weak texture. This study was able to achieve a maximum strain of 0.01 and a maximum stress of 500 MPa. This is in comparison to Dong [19] that was able to achieve a maximum compressive elastic strain of 0.01 and 50 MPa before buckling occurred in snap-fit Ti-6Al-4 V trusses. This shows a considerable increase in maximum stress of the octet truss unit cell manufactured by additive manufacturing out of Ti-5553.

## 5. Conclusion

This study has presented direct measurements of the effective elastic properties of an additively manufactured titanium alloy octet truss unit cell. The samples were loaded in compression and crystallographic lattice strains were measured using high energy X-ray diffraction. The microstructure of the sample was also characterized using a suite of techniques.

There are several key takeaways from the study:

- The microstructure featured a weak texture but a significant amount of porosity in the as-printed state. The porosity grew to 0.39% of the sample volume by the end of compression. A secondary phase, likely orthorhombic martensite Ti, was found in the sample near the nodes.

There were no large voids at the initial fracture site. There were several possible mechanisms for failure including microvoid coalescence, cleavage on a grain boundary, and crack initiation from surface roughness.

- The principal tensile strains of the sample were primarily concentrated in horizontal struts (1 and 8, Fig. 1) that were located in the middle of the sample. Likewise, the principal compressive strains were concentrated in diagonal struts (4 and 7, Fig. 1) in the middle of the sample. These four struts were the only members that were not pinned by at least one node. These struts showed stiffness values very close to the elastic stiffness of the material.
- The deformation of the octet truss unit cell was best described by an orthorhombic linear elastic relationship. The deviation from an isotropic response, as predicted by Deshpande, Fleck and Ashby, can be explained by two primary causes. A major assumption of the DFA model is that all nodes in the sample are pin jointed, as is the case for a many-unit-cell sample. This study investigated a single unit cell that had only the top and bottom nodes pinned. Furthermore, the sample had a myriad of defects throughout. Inhomogeneities in the distribution of these defects likely caused a unique stress-strain response in each strut observed.

These results present the opportunity to further characterize octet truss unit cells using high energy X-ray diffraction. The technique used herein can be applied to other combinations of unit cells, so long as the X-ray beam can be trained on a single spot in the sample without hitting another strut in its path. This opens up the door for directly characterizing the effective elastic properties of other octet truss structures and parts with many unit cells as well as other lattice topologies. These types of studies afford the chance to directly compare between experimental results on the unit cell scale and the macroscale, as well as compare against model predictions and the robust theory that exists for these structures.

## CRediT authorship contribution statement

**Nathan S. Johnson:** Conceptualization, Data curation, Formal analysis, Investigation, Methodology, Project administration, Software, Validation, Visualization, Writing – original draft, Writing – review & editing. **Maria Strantza:** Data curation, Formal analysis, Investigation, Methodology, Resources. **Manyalibo J. Matthews:** Conceptualization, Funding acquisition, Investigation, Project administration, Resources. **Jun-Sang Park:** Investigation, Methodology, Resources. **Peter Kenesei:** Investigation, Methodology, Resources. **Bjørn Clausen:** Conceptualization, Formal analysis, Investigation, Methodology, Resources, Software. **Donald W. Brown:** Conceptualization, Data curation, Formal analysis, Funding acquisition, Investigation, Methodology, Project administration, Resources, Supervision, Validation, Writing – review & editing. **John S. Carpenter:** Conceptualization, Funding acquisition, Investigation, Methodology, Project administration, Resources, Supervision, Validation, Writing – original draft, Writing – review & editing. **Craig A. Brice:** Supervision, Writing – original draft. **Aaron P. Stebner:** Conceptualization, Data curation, Formal analysis, Investigation, Methodology, Resources, Supervision, Writing – original draft, Writing – review & editing.

## Declaration of competing interest

The authors declare that they have no known competing financial interests or personal relationships that could have appeared to influence the work reported in this paper.

## Data availability

All data, and python code, is included in the supplementary material.

## Acknowledgements

This research used resources of the Advanced Photon Source, a U.S. Department of Energy (DOE) Office of Science user facility at Argonne National Laboratory and is based on research supported by the U.S. DOE Office of Science-Basic Energy Sciences, under Contract No. DEAC02-06CH11357. This work was supported by the U.S. Department of Energy through the Los Alamos National Laboratory. Los Alamos National Laboratory is operated by Triad National Security, LLC, for the National Nuclear Security Administration of U.S. Department of Energy (Contract No. 89233218CNA000001). This work was performed under the auspices of the U.S. Department of Energy by Lawrence Livermore National Laboratory under Contract DE-AC52-07NA27344.

## Appendix A. Supplementary data

Supplementary data to this article can be found online at <https://doi.org/10.1016/j.matchar.2024.113755>.

## References

- [1] D. Mahmoud, M.A. Elbestawi, *J. Manuf. Mater. Process.* 1 (2017) 2.
- [2] X. Zhang, M. Leary, H. Tang, T. Song, M. Qian, *Curr. Opin. Solid State Mater. Sci.* 22 (2018) 75.
- [3] M.A. El-Sayed, K. Essa, M. Ghazy, H. Hassanin, *Int. J. Adv. Manuf. Technol.* 110 (2020) 2257.
- [4] N. Soro, E.G. Brodie, A. Abdal-hay, A.Q. Alali, D. Kent, M.S. Dargusch, *Mater. Des.* 218 (2022).
- [5] G. Totaro, Z. Gurdal, *Aerospace Sci. Technol.* 13 (2009) 157.
- [6] J.C. Najmon, S. Raeisi, A. Tovar, 2-Review of Additive Manufacturing Technologies and Applications in the Aerospace Industry vol. 1, Elsevier, 2019.
- [7] M. Abdi, I. Ashcroft, R. Wildman, *Int. J. Powertrains* 1 (1) (2018).
- [8] Z. Ozdemir, E. Hernandez-Nava, A. Tyas, J.A. Warren, S.D. Fay, R. Goodall, I. Todd, H. Askes, *Int. J. Impact Eng.* 89 (2016) 49.
- [9] F. Habib, P. Iovenitti, S. Masood, M. Nikzad, *Mater. Des.* 155 (2018) 86.
- [10] K.J. Maloney, K.D. Fink, T.A. Schaedler, J.A. Kolodziejska, A.J. Jacobsen, C. S. Roper, *Int. J. Heat Mass Transf.* 55 (2012) 2486.
- [11] V. Deshpande, N. Fleck, M. Ashby, *J. Mech. Phys. Solids* 49 (2001) 1747.
- [12] V. Deshpande, M. Ashby, N. Fleck, *Acta Mater.* 49 (2001) 1035.
- [13] W. Lv, D. Li, L. Dong, *Compos. Struct.* 249 (2020).
- [14] S.O. Obadim, K.I. Kourousis, *Aerospace* 8 (2021).
- [15] A. Moussa, D. Melancon, A.E. Elm, D. Pasini, *Addit. Manuf.* 37 (2021).
- [16] L. Dong, V. Deshpande, H. Wadley, *Int. J. Solids Struct.* 60 (2015) 107.
- [17] L. Dong, H. Wadley, *Compos. Sci. Technol.* 119 (2015) 26.
- [18] L. Dong, H. Wadley, *Compos. A: Appl. Sci. Manuf.* 81 (2016) 182.
- [19] L. Dong, *Mater. Des.* 208 (2021).
- [20] A. Vigliotti, V.S. Deshpande, D. Pasini, *J. Mech. Phys. Solids* 64 (2014) 44.
- [21] R.N. Glaesener, E.A. Traff, B. Telgen, T.M. Canonica, D.M. Kochmann, *Int. J. Solids Struct.* 206 (2020) 101.
- [22] H. Schwab, F. Palm, U. Kuhn, J. Eckert, *Mater. Des.* 105 (2016) 75.
- [23] S.K. Kar, A. Ghosh, N. Fulzele, A. Bhattacharjee, *Mater. Charact.* 81 (2013) 37.
- [24] R. Boyer, R. Briggs, J. Mater. Eng. Perform. 14 (2005) 681.
- [25] T. Grove, B. Denkena, O. Maiß, A. Krodel, H. Schwab, U. Kuhn, *J. Mech. Sci. Technol.* 32 (2018) 4883.
- [26] R. Ganeriwala, M. Strantza, W. King, B. Clausen, T. Phan, L. Levine, D. Brown, N. Hodge, *Addit. Manuf.* 27 (2019) 489.
- [27] A.C. Konstantinidis, M.B. Szafraniec, R.D. Speller, A. Olivo, *Nuclear instruments and methods in physics research section a: accelerators, Spectromet. Detect. Assoc. Equip.* 689 (2012) 12.
- [28] Advanced Photon Source, Compact Load Frame, URL, <https://www.aps.anl.gov/Sector-1-ID/Infrastructure/Compact-load-frameID>, 2024.
- [29] B. Toby, R. Von Dreele, *J. Appl. Crystallogr.* 46 (2013) 544.
- [30] Object Research Systems (ORS) Inc, Montreal, Canada, Software available at, <http://www.theobjects.com/dragonfly>, 2020.
- [31] G. Ischia, H.-R. Wenk, L. Lutterotti, F. Berberich, *J. Appl. Crystallogr.* 38 (2005) 377.
- [32] F. Bachmann, R. Hielscher, H. Schaeben, *Solid State Phenom.* 160 (2010) 63.
- [33] A. Larson, R. Von Dreele, General Structure Analysis System (GSAS), Los Alamos National Laboratory, 2000. Report LAUR 86-748.
- [34] B. Clausen, SMARTSwear Manual vol. LA-UR 04-6581, 2004. Los Alamos, NM, <http://public.lanl.gov/clausen/smartsware.html>.
- [35] I. Noyan, J. Cohen, *Residual Stress: Measurement by Diffraction and Interpretation* 1st ed., vol. 1, Springer-Verlag, New York, 1987.
- [36] A.M. Korsunsky, K.E. Wells, P.J. Withers, *Scr. Mater.* 39 (1998) 1705.
- [37] D. Brown, A. Losko, J. Carpenter, J. Cooley, B. Clausen, J. Dahal, P. Kenesei, J.-S. Park, *Metall. Mater. Trans. A* 50 (2019) 2538–2553.
- [38] M. Strantza, R. Ganeriwala, B. Clausen, T. Phan, L. Levine, D. Pagan, J. Ruff, W. King, N. Johnson, R. Martinez, et al., *Addit. Manuf.* 45 (2021).
- [39] N. Clément, Ph.D. thesis, Universite Catholique De Louvain, Louvain-la-Neuve, 2010.
- [40] B.N. Taylor, C.E. Kuyatt, *NIST Technical Note* 1297, 1994. Edition.
- [41] Y. Zheng, R.E. Williams, H.L. Fraser, *Scr. Mater.* 113 (2016) 202.
- [42] D. Greitemeier, C.D. Donne, F. Syassen, J. Eufinger, T. Melz, *Mater. Sci. Technol.* 32 (2016) 629.
- [43] A.R. Torrado, D.A. Roberson, *J. Fail. Anal. Prev.* 16 (2016) 154.
- [44] M. Tang, P.C. Pistorius, *JOM* 69 (2017).
- [45] G. Bean, T. McLouth, D. Witkin, S. Sitzman, P. Adams, R. Zaldivar, *J. Mater. Eng. Perform.* 28 (2019) 1942.
- [46] T.G. Gallmeyer, S. Moorthy, B.B. Kappes, M.J. Mills, B. Amin-Ahmadi, A. P. Stebner, *Addit. Manuf.* 31 (2020).
- [47] M. Bache, W. Evans, *Mater. Sci. Eng. A* A319-321 (2001) 409.
- [48] M. Simonelli, Y. Tse, C. Tuck, *Mater. Sci. Eng. A* 616 (2014) 1.
- [49] Y. Kok, X. Tan, P. Wang, M. Nai, N. Loh, E. Liu, S. Tor, *Mater. Des.* 139 (2018) 565.
- [50] M. Strantza, R. Ganeriwala, B. Clausen, T. Phan, L. Levine, D. Pagan, W. King, N. Hodge, D. Brown, *Mater. Lett.* 231 (2018) 221.
- [51] B.B. Babamiri, J. Indeck, G. Demeneghi, J. Cuadra, K. Hazeli, *Addit. Manuf.* 34 (2020).
- [52] Y. Liu, X. Li, L. Zhang, T. Sercombe, *Mater. Sci. Eng. A* 642 (2015) 268.
- [53] A. Dressler, E. Jost, J. Miers, D. Moore, C. Seepersad, B. Boyce, *Addit. Manuf.* 28 (2019) 692–703.
- [54] L. Delcuse, S. Bahi, U. Gunputh, A. Rusinek, P. Wood, M. Miguelez, *Addit. Manuf.* 36 (2020).
- [55] E.W. Jost, D.G. Moore, C. Saldanaa, *Addit. Manuf. Lett.* 1 (2021) 1.